nature nanotechnology

Article

https://doi.org/10.1038/s41565-023-01325-2

Single-photon detection using high-temperature superconductors

Received: 11 May 2022

Accepted: 10 January 2023

Published online: 20 March 2023



I. Charaev $\textcircled{0}^{1,2,8} \boxtimes$, D. A. Bandurin $\textcircled{0}^{3,8} \boxtimes$, A. T. Bollinger $\textcircled{0}^4$, I. Y. Phinney¹, I. Drozdov $\textcircled{0}^4$, M. Colangelo $\textcircled{0}^1$, B. A. Butters $\textcircled{0}^1$, T. Taniguchi $\textcircled{0}^5$, K. Watanabe $\textcircled{0}^6$, X. He^{4,7}, O. Medeiros¹, I. Božović $\textcircled{0}^{4,7}$, P. Jarillo-Herrero $\textcircled{0}^1$ & K. K. Berggren $\textcircled{0}^1 \boxtimes$

The detection of individual quanta of light is important for quantum communication, fluorescence lifetime imaging, remote sensing and more. Due to their high detection efficiency, exceptional signal-to-noise ratio and fast recovery times, superconducting-nanowire single-photon detectors (SNSPDs) have become a critical component in these applications. However, the operation of conventional SNSPDs requires costly cryocoolers. Here we report the fabrication of two types of high-temperature superconducting nanowires. We observe linear scaling of the photon count rate on the radiation power at the telecommunications wavelength of 1.5 µm and thereby reveal single-photon operation. SNSPDs made from thin flakes of Bi₂Sr₂CaCu₂O_{8+δ} exhibit a single-photon response up to 25 K, and for SNSPDs from La_{1.55}Sr_{0.45}CuO₄/La₂CuO₄ bilayer films, this response is observed up to 8 K. While the underlying detection mechanism is not fully understood yet, our work expands the family of materials for SNSPD technology beyond the liquid helium temperature limit and suggests that even higher operation temperatures may be reached using other high-temperature superconductors.

The detection of individual light quanta is critical for a broad range of applications in both quantum and classical realms. Quantum computation¹⁻⁶, metrology⁷⁻⁹, secure communication¹⁰⁻¹³, single-photon imaging¹⁴⁻¹⁶, single-molecule detection¹⁷, remote sensing^{18,19} and correlation spectroscopy^{20,21} are just a short list of applications where faint light detectors play a crucial role. At present, the technology of single-photon detection is predominantly enabled by photomultiplier tubes, single-photon avalanche diodes, visible-light photon counters and superconducting detectors ²²⁻²⁵. In particular, superconducting-nanowire single-photon detectors (SNSPDs, also sometimes simply SSPDs) stand out in terms of broadband operation²⁶ with high detection efficiency²⁷⁻²⁹, exceptional signal-to-noise

ratio³⁰, ultra-high temporal resolution³¹ and fast recovery time³². These exceptional characteristics are enabled by the physics behind SNSPD operation which is based on the generation of an electrical signal (voltage pulse) triggered by the local suppression of the superconducting state upon photon absorption in a current-biased superconducting nanowire (SNW)³³. The formation of such a non-superconducting region (hot-spot) leads to the local reduction of the maximum (critical) supercurrent. If the bias current, I_{bias} , exceeds the critical value for this region, the SNW transitions to the resistive state, leading to the voltage spike³⁴.

The idea of using the nonlinearity of the superconductor-to-metal phase transition for detection dates back to the 1960s when SNWs were proposed as a sensitive tool to detect elementary particles³⁵. The

¹Massachusetts Institute of Technology, Cambridge, MA, USA. ²University of Zurich, Zurich, Switzerland. ³Department of Materials Science and Engineering, National University of Singapore, Singapore, ⁴Brookhaven National Laboratory, Upton, NY, USA. ⁵International Center for Materials Nanoarchitectonics, National Institute of Material Science, Tsukuba, Japan. ⁶Research Center for Functional Materials, National Institute of Material Science, Tsukuba, Japan. ⁷Department of Chemistry, Yale University, New Haven, CT, USA. ⁸These authors contributed equally: I. Charaev, D. A. Bandurin. ⊠e-mail: ilya.charaev@physik.uzh.ch; bandurin.d@gmail.com; berggren@mit.edu

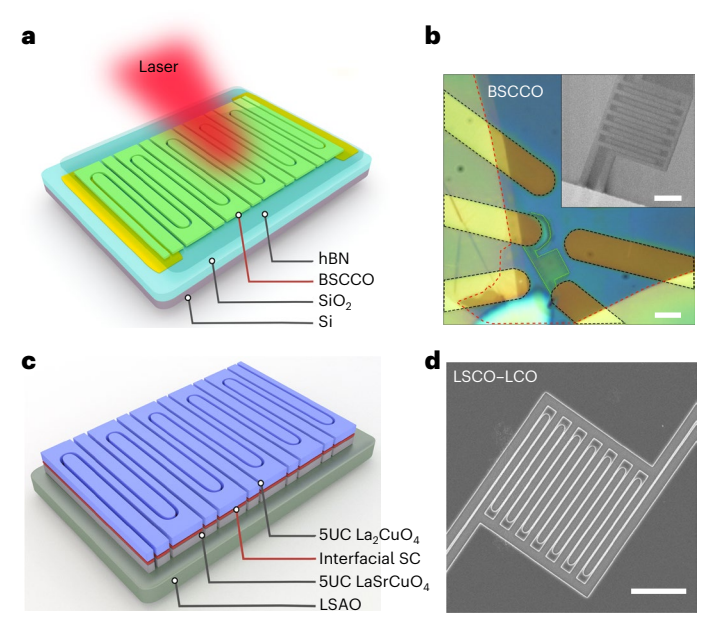


Fig. 1| **High-** T_c **superconducting nanowires. a**, Schematic of the BSCCO single-photon detector: a relatively thin flake of BSCCO is covered by a much thicker flake of hBN and transferred onto ultra-flat gold contacts. The SNW region is defined by a He⁺ beam exposure. **b**, Optical photograph of the BSCCO device. The green line demarcates the photodetector area. The contact geometry was chosen to reduce the total resistance of the gold electrodes. Scale bar, 3 μm. Inset: example SEM image of a BSCCO SNW produced by He⁺ beam exposure (similar but not identical to that from the photograph: to avoid degradation, we refrained from characterizing the photodetector using SEM imaging). Scale bar, 2 μm. **c**, Schematic of the LSCO–LCO single-photon detector: a high- T_c two-dimensional superconductor (SC) is formed at the interface between the 5-UC-thick layer of the LCO insulator and the 5-UC-thick layer of the LSCO metal on strontium lanthanum aluminate (LSAO) substrate. The contact leads are 50-nm-thick titanium–gold. **d**, An SEM image of a typical LSCO–LCO SNW device. Scale bar, 2 μm.

evolution of this proposal led to the development of sensitive bolometers based on SNWs made out of niobium nitride (NbN) thin films³⁶, followed by a successful demonstration of the single-photon detection regime that gave birth to SNSPD technology^{37,38}. At present, SNSPDs require the use of costly and bulky cryocoolers to bring the SNWs below the liquid helium temperatures where the superconducting state of the SNW is well developed. For this reason, for the past two decades, there has been a continuous exploration of other superconductors with higher critical temperatures, T_c , that would allow for single-photon detection at elevated T (ref. 39). This search proved to be exceedingly challenging, and only one promising candidate has emerged so far: in SNSPDs made of MgB₂ thin films with $T_c = 30$ K, the single-photon response in the optical range was demonstrated at $T \approx 10$ K (ref. ⁴⁰). Surprisingly, with few exceptions 41-43, cuprate superconductors remain largely unexplored in this context in spite of their record-high T_c . The reason lies in the technological challenge to produce SNW devices out of thin cuprate films-most of which rapidly degrade upon conventional nanofabrication processing. Indeed, attempts to realize SNSPD out of YBa₂Cu₃O_{7-x} SNWs revealed no single-photon response even at liquid helium temperatures 41,42,44-46. In this work, we demonstrate SNSPDs fabricated out of two high- T_c cuprate superconductors, $Bi_2Sr_2CaCu_2O_{8+\delta}$ $(BSCCO)^{47,48}$ and $La_{2-x}Sr_xCuO_4$ (LSCO).

Design and characterization of the cuprate nanowires

To fabricate SNWs out of BSCCO, we mechanically exfoliated bulk BSCCO crystals to produce relatively thin flakes. To protect the flakes from the environment, the exfoliation was performed in the inert

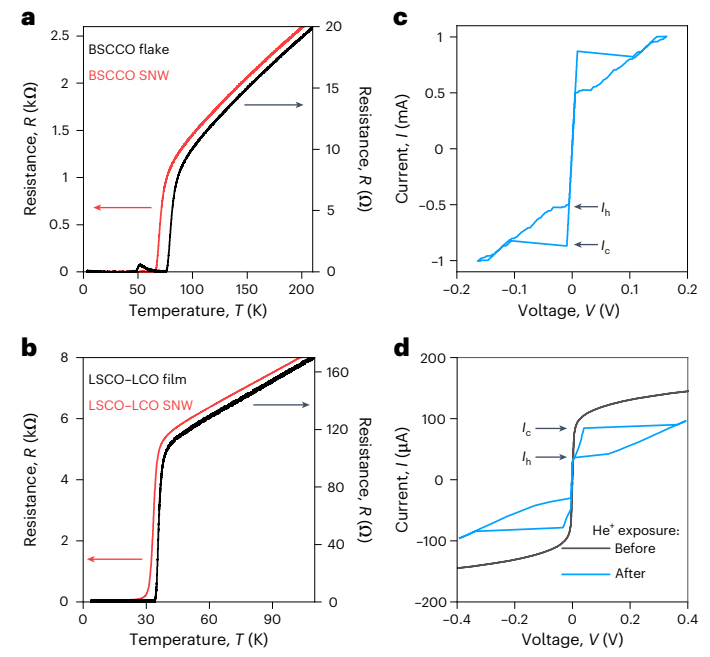


Fig. 2 | **Transport properties of cuprate SNWs. a,b**, Examples of the R(T) dependencies for BSCCO (a) and LSCO–LCO (b) flake, film and SNWs. \mathbf{c} , I–V curve for BSCCO SNWs measured at T = 3.7 K in the four-terminal configuration. \mathbf{d} , Typical I–V curves of LSCO–LCO SNWs measured in the two-terminal configuration at T = 3.7 K before and after He $^+$ ion exposure.

atmosphere of an argon-filled glovebox. The flakes were transferred onto prepatterned ultra-flat gold contacts and covered with relatively thin slabs of hexagonal boron nitride (hBN) as illustrated in Fig. 1a. We intentionally focused on 10-15 nm thick slabs (Fig. 1a) because ultra-thin BSCCO flakes are prone to faster degradation^{49–51}. Thicker flakes also facilitate stronger absorption of incident light while maintaining quasi-two-dimensional superconductivity. Nevertheless, even few-unit-cell flakes are not amenable to standard nanofabrication processes, since their doping level changes upon contact with the environment, rendering the sample non-superconducting 49,52,53. To circumvent this, we used a He⁺ ion beam to define the SNW patterns by introducing defects into the encapsulated BSCCO flake, causing the exposed regions to become insulating^{54–57} (Fig. 1b). In contrast to patterning with heavier ions (for example, gallium or xenon), the exposed regions were not etched under He⁺ beam irradiation. The inset of Fig. 1b shows a typical scanning electron microscopy (SEM) image of a partially encapsulated BSCCO flake after the He⁺ patterning: a meander-like SNW can be seen due to the enhanced contrast of the exposed regions. The total length of the BSCCO SNW was 56 µm whereas its width was of the order of 100 nm. See Supplementary Information, section 1 for further details.

For successful implementation of the high-temperature SNSPD technology, it is critical to ensure large-scale production of thin high- $T_{\rm c}$ films and their patterning using conventional nanofabrication processes. For these reasons, in this work we have also explored thin La_{1.55}Sr_{0.45}CuO₄/La₂CuO₄ (LSCO–LCO) bilayer films. These heterostructures offer several advantages. First, high-quality LSCO–LCO bilayer films can be grown using atomic-layer-by-layer molecular beam epitaxy (ALL-MBE)^{58,59} (Supplementary Information, section 2). Second, while in such bilayers neither constituent material is superconducting—LCO is an insulator and LSCO is a non-superconducting metal—the heterostructure shows high- $T_{\rm c}$ interface superconductivity confined to a single CuO₂ plane^{58,59}. Thus, using such heterostructures, high- $T_{\rm c}$ SNWs can be fabricated with the cross section reduced by two orders

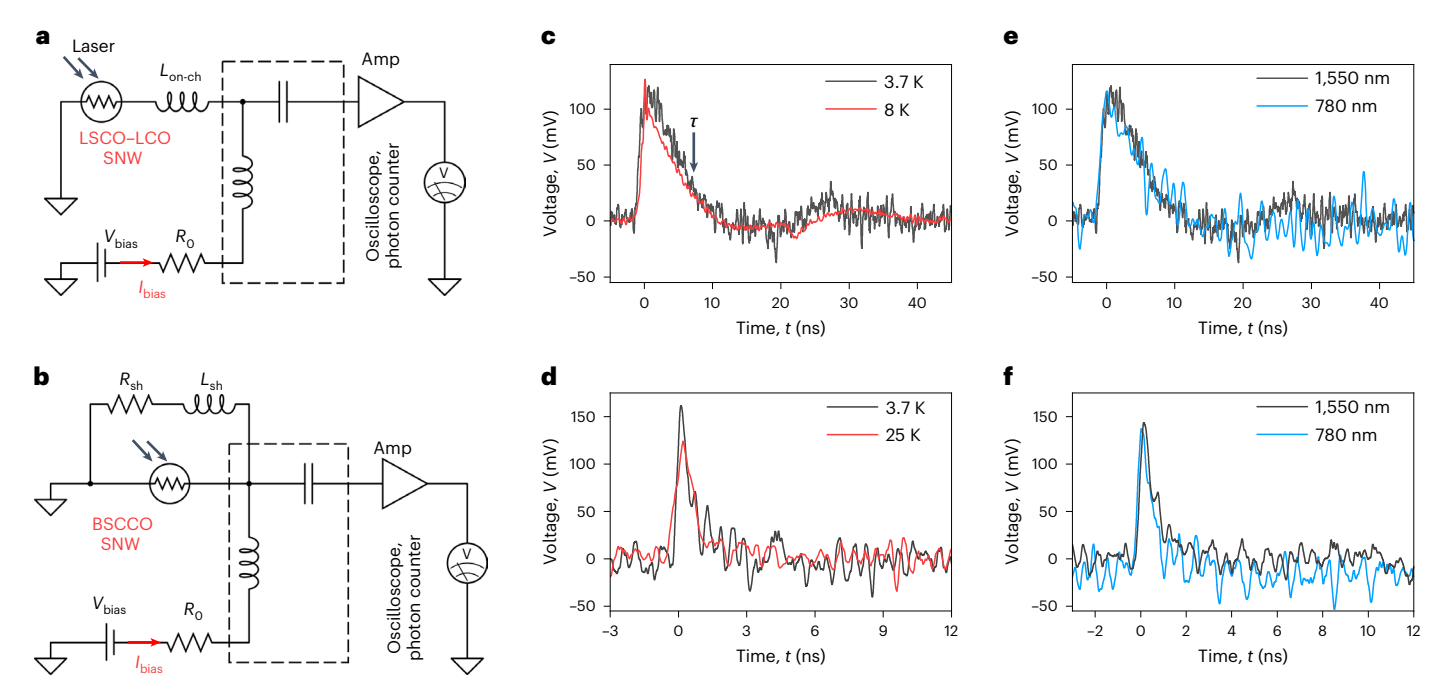


Fig. 3 | **Photovoltage generation in cuprate SNW detectors. a**, Simplified circuit diagram used to measure the photoresponse of the LSCO–LCO SNW detector. The SNW is current-biased by an isolated voltage source connected to the d.c. port of the bias tee (dashed rectangle) through an R_0 = $100 \, \mathrm{k}\Omega$ resistor. Incident radiation triggers a voltage spike generating a short pulse that propagates through the a.c. port of the bias tee to the preamplifier and is read out using an oscilloscope or a photon counter. $L_{\mathrm{on-ch}} \approx 310 \, \mathrm{nH}$ is an on-chip kinetic inductor made out of the LSCO–LCO film. **b**, Simplified circuit diagram used

to measure the photoresponse of the BSCCO SNW detector. $R_{\rm sh}/L_{\rm sh}\approx 45$ MHz. Details of the shunt circuitry can be found elsewhere (for example, refs. 62,63). **c.d.** Photovoltage $V_{\rm ph}$ pulses measured in the LSCO–LCO (**c**) and BSCCO (**d**) photodetectors at given T and $\lambda=1.5$ µm. The devices are biased to 95% of their critical current for given T. The recovery time (τ) is shown by black arrow. **e.f.**, Photovoltage $V_{\rm ph}$ pulses measured at given λ for the LSCO–LCO (**e**) and BSCCO (**f**) devices at T=3.7 K and T=16 K, respectively.

of magnitude, among the smallest of any SNW so far reported. Finally, LSCO–LCO bilayers are stable in air for years, and resilient to degradation during standard lithography, etching and contact deposition processes. In this work, we used heterostructures comprised of a 5-unit-cell (UC)-thick layer of LCO grown on top of a 5-UC-thick layer of LSCO (Fig. 1c). We used the electron-beam lithography to define an SNW meander structure typical for SNSPDs, 60 μ m in length and 100 nm in width, with a filling factor 0.28 (Fig. 1d). For the fabrication details, see Methods and Supplementary Information, section 2.

After fabrication, we characterized the transport properties of our high- T_c SNWs. Figure 2a,b shows the typical temperature dependence of the resistance, R(T), of SNWs fabricated out of BSCCO and LSCO–LCO, revealing their respective critical temperatures of 69.8 K and 34.4 K as determined from the maximum of dR/dT(T). The obtained values are somewhat lower than those obtained for the parent BSCCO flake and LSCO–LCO bilayer film, that is, 79.8 K and 35.5 K, respectively (Fig. 2a,b, black traces). This indicates a mild degradation of the materials' superconducting properties during the fabrication. BSCCO underwent a more substantial change in T_c , probably because of its much stronger sensitivity to the environment.

An important characteristic of most SNWs, enabling the generation of a voltage pulse upon single-photon absorption, is the metastable state that emerges under current biasing 60 . This metastable state appears due to the competition between the current-induced Joule self-heating of the SNW in the normal state and electron cooling processes, and manifests itself as a pronounced hysteresis on the I-V characteristics. Figure 2c shows a typical I-V curve measured in our BSCCO device below T_c when the SNW is current-biased. A clear hysteretic behaviour characterized by the switching current $I_c = 883 \, \mu A$ and the retrapping current $I_h = 516 \, \mu A$ is observed. The I-V curves of the as-prepared LSCO–LCO SNWs were, however, hysteresis-free and

thus these SNWs were not suitable for a single-photon detector per se (Fig. 2d). To circumvent this problem, we exposed the device to a relatively small dose of ${\rm He^+ions^{56}}\,(10^{16}\,{\rm cm^{-2}})$ (Supplementary Information, section 3). Such exposure had only a mild effect on I_c , T_c and the normal state R_s ; however, it led to the desired I-V hysteresis with I_c = 86.7 $\mu{\rm A}$ and I_h = 36.3 $\mu{\rm A}$ (Fig. 2d and Supplementary Information, section 4). The origin of I-V hysteresis in the exposed LSCO–LCO bilayer SNWs is yet to be understood; we tentatively attribute it to the modification of the electron cooling rate caused by the introduced defects.

Photoresponse measurements

To perform the photoresponse measurements, we mounted our cuprate SNWs in a variable-temperature cryostat equipped with radiofrequency coax cables and an optical fibre. The latter was held approximately 1 cm away from the device so that a defocused continuous-wave laser beam covered the entire device area. The cooling power of our cryogenic set-up significantly exceeds the power of incident laser radiation, ensuring the thermal stability of our samples upon illumination. The simplified circuit diagrams, used for the photoresponse measurements, are shown in Fig. 3a,b. The LSCO-LCO device was measured in a conventional SPD configuration in which the SNW was biased through a d.c. input of the bias tee using an isolated voltage source connected in series with a resistor, R_0 . The a.c. output was connected to a low-noise amplifier, the output of which was fed to an oscilloscope or a photon counter (Fig. 3a). To mitigate latching effects in this superconducting photodetector, the SNW was connected in series with an on-chip kinetic inductor, Lon-ch, also made out of the superconducting LSCO-LCO bilayer 14,61,62 . The BSCCO measurement configuration was somewhat similar, but in this case, we used a more conventional low-frequency reset loop formed by an inductor, L_{sh} , and a resistor, R_{sh} , connected in series with each other⁶³ (Fig. 3b).

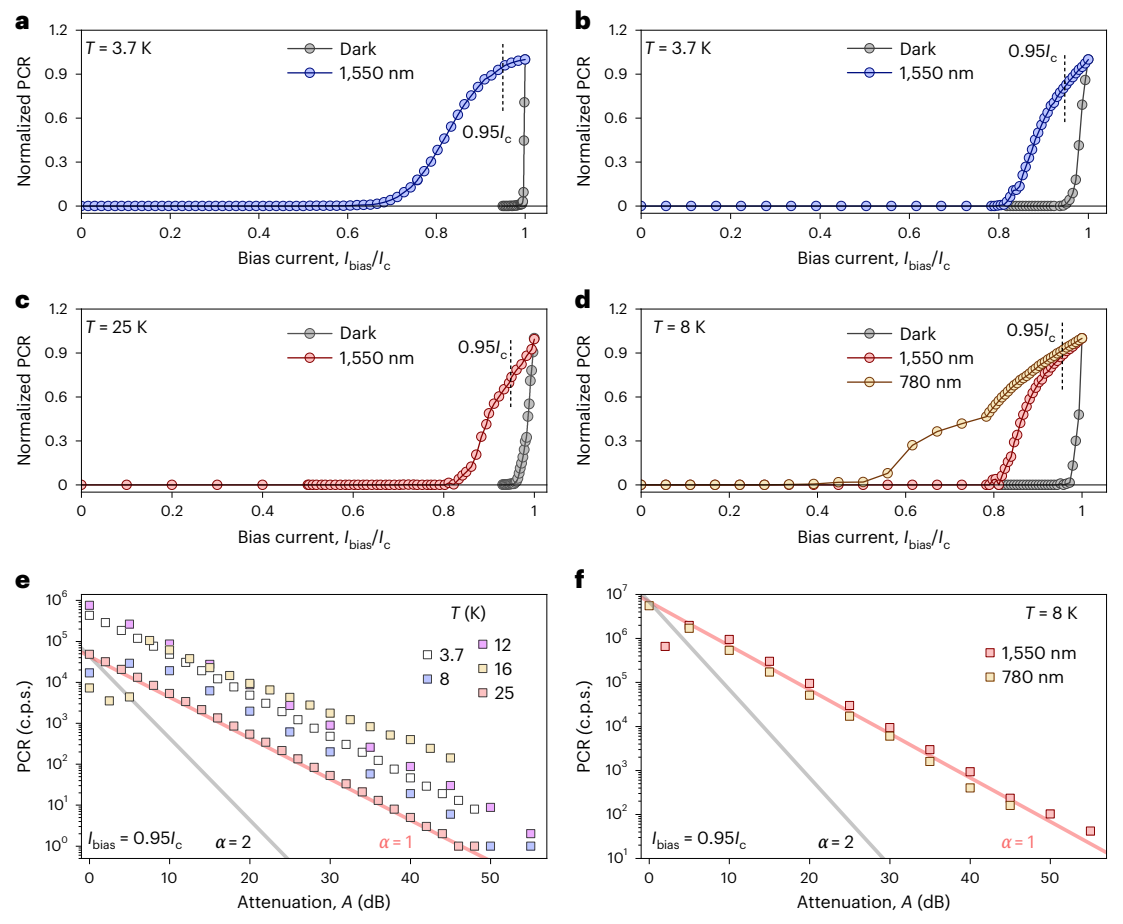


Fig. 4 | **Single-photon detection by cuprate SNWs. a,b**, PCR normalized to its maximum value as a function of bias current, $I_{\rm bias}$, measured in the BSCCO (**a**) and LSCO–LCO (**b**) photodetectors in the dark and upon illumination with λ = 1.5 µm light. **c**, The same as **a** but for T = 25 K. **d**, Normalized PCR versus $I_{\rm bias}$ for different λ measured in the LSCO–LCO device at T = 8 K. Vertical dashed lines in **a**–**d** show $I_{\rm bias}$ corresponding to 95% of the switching current at T = 3.7 K. **e**, PCR versus attenuation factor, A, at different T for the BSCCO device at given $I_{\rm bias}$, λ = 1.5 µm.

Note: to avoid overheating the BSCCO SNW at T=25 K we intentionally reduced the initial output power of the laser, P_0 , which resulted in the shift of the PCR(A) dependence towards smaller count rates. **f**, PCR versus A dependencies for the LSCO–LCO devices measured at given λ and I_{bias} , T=8 K. c.p.s., counts per second. Red and black lines in **e** and **f** are guides to the eye showing PCR $\approx P_{\text{inc}}^{\alpha}$ scaling for the single-photon ($\alpha=1$) and multiphoton ($\alpha>1$, e.g. $\alpha=2$ as shown on the graph) regimes, respectively.

Figure 3c shows an example of the photovoltage generation, $V_{\rm ph}$, measured across the current-biased LSCO-LCO SNWs when the device was exposed to laser beam radiation of wavelength $\lambda = 1.5 \,\mu\text{m}$. The $V_{\text{ph}}(t)$ traces of this SNW shared common features with the photoresponse of conventional SNSPDs. After photon absorption, $V_{ph}(t)$ spikes and quickly reaches its maximum value. This is followed by a much slower decay with the characteristic time t, often referred to as dead or recovery time, which depends on the total kinetic inductance, L_k , of the superconducting circuit⁶⁴. The measured value, $\tau \approx 7$ ns (determined as the time when the signal dropped to 30% of its maximum value) is in agreement with our measurements of the kinetic inductance in the LSCO-LCO bilayer films (Supplementary Information, section 5). The $V_{\rm ph}$ spikes in the LSCO–LCO SNW device were observed below and above the liquid helium temperature and could be detected up to T = 8 K. At higher T, LSCO-LCO SNWs did not exhibit an I-V hysteresis, and thus no voltage pulses were observed upon illuminating the SNW with low-intensity laser light (Supplementary Information, section 4).

As compared to LSCCO–LCO, the $V_{\rm ph}$ pulses in biased BSCCO SNWs were observed up to much higher T=25 K (Fig. 3d), above which the I-V hysteresis disappeared (Supplementary Information, section 4). The spikes were characterized by a much faster recovery time $\tau\approx0.8$ ns. We attribute this short τ to a smaller total kinetic inductance of the BSCCO photodetector (Supplementary Information, section 5). We have also

tested the dependence of $V_{\rm ph}$ on the photon energy and found that the LSCO–LCO and BSCCO SNWs yielded spikes at both λ = 1.5 μ m and λ = 780 nm (Fig. 3e,f). Finally, we note that above the critical current our devices latch, and therefore do not feature voltage pulses on an oscilloscope and corresponding counts on a photon counter.

Single-photon sensitivity of the cuprate photodetectors

To get further insight into the performance of our cuprate photodetectors, we recorded the photon count rate, PCR (the number of $V_{\rm ph}$ pulses per unit time), as a function of the bias current, I_{bias} . Figure 4a shows the PCR normalized to its maximum value, measured in our BSCCO device in the dark and upon exposing it to the $\lambda = 1.5 \,\mu m$ laser light. In the dark, spontaneous voltage pulses emerge close to the critical current, a typical behaviour of SNSPDs. The absolute value of these dark counts did not exceed 10³ s⁻¹, comparable to the values in conventional NbN SNSPDs. Upon illumination, the counts appeared at much lower onset current $I_{\text{bias}} = 0.62I_{\text{c}}$, whereas the PCR showed some tendency to saturation upon approaching I_c . This saturation indicates high internal detector efficiency⁶⁵. With increasing T to 25 K, the onset current decreased together with I_c , as expected for conventional SNSPDs (Fig. 4c). Furthermore, we found that the PCR for a given I_{bias} was almost independent of λ and featured similar PCR(I_{bias}) functional dependencies for $\lambda = 780$ nm and $\lambda = 1.5$ µm (Supplementary Information, section 6). We observed zero PCR on devices made out of non-optimally doped BSCCO flakes; the latter exhibited only signatures of the bolometric photoresponse (Supplementary Information, section 6).

The PCR– $I_{\rm bias}$ characteristics obtained for the LSCO–LCO photodetector at $\lambda=1.5~\mu m$ were rather similar to those for BSCCO yet the counts emerged at much smaller $I_{\rm bias}$ due to a smaller critical current in this SNW (Fig. 4b,d). The onset current was about 0.75 $I_{\rm c}$ for both T=3.7 and 8 K. Notably, upon decreasing λ to 780 nm, the functional form of the PCR($I_{\rm bias}$) scaling changed drastically and featured a rather unusual dependence (Fig. 4d). First, the counts appeared at much lower $I_{\rm bias}\approx 20~\mu A$. Then, the PCR exhibits a tendency to saturation on increasing $I_{\rm bias}$ to $\sim 52~\mu A$. Finally, above this value, the PCR started to ascend again, suggesting two distinct operation modes of the LSCO–LCO photodetector.

While the data support the hypothesis of single-photon detection in these two materials, a number of features of the data are different from the observations in SNSPDs in conventional superconductors. Specifically: (1) we observed unusual I-V characteristics in hysteretic LSCO–LCO SNWs (Fig. 2d); (2) we observed at one temperature (16 K) α <1 slope in the PCR(A) curve for BSSCO at high A; and (3) we observed unusual structure in the PCR($I_{\rm bias}$) curves for the LSCO–LCO SNSPD. Given the early stage of development of materials processing used in this work, such anomalies are not unexpected. While our high- $T_{\rm c}$ films are homogeneous, we expect non-uniformity in the patterning and processing, so different regions of the SNWs could be participating in the detection process at different T, λ and $I_{\rm bias}$.

Next, in Supplementary Information, section 7, we provide estimates for the BSCCO detector efficiency, DE. To this end, we used experimentally determined absorption of thin BSCCO flakes deposited onto ${\rm SiO_2}$ substrate⁴⁹. We found that at 25 K, at which PCR is - 10^4 s⁻¹ for the 10 dB attenuation, the DE is of the order of 1.5%. Note, these estimates are crude as they do not account for interference effects in ${\rm SiO_2}$ and hBN, typical for 2D heterostructures, which can lead to enhancement and reduction of the apparent efficiency. Nevertheless, we envision that DE can be boosted by integrating the SNSPDs into photonic cavities providing enhanced light–matter interaction.

Finally, we consider the microscopic processes governing the single-photon response in cuprate SNWs. In general, the absorption of a photon by the SNW leads to the excitation of one electron into an empty state in the conduction band above the superconducting gap. This excited electron relaxes and disturbs the superconducting equilibrium state, leading to the formation of a normal domain. While the hot-spot dynamics in the current-biased SNWs is qualitatively understood, an accurate theoretical description of the hot-spot evolution lacks completeness⁶⁶. Nevertheless, all existing models rely on a set of parameters inherent to a parent superconductor: for example, coherence length, penetration depth, electron-phonon coupling strength, diffusion coefficient, and specific heat capacities of electrons and phonons. Superconductors proven to work in the SNSPDs showed minor variations in these characteristics. However, the properties of unconventional cuprate superconductors are drastically different in both superconducting and normal phases⁶⁷⁻⁶⁹. First, cuprates are d-wave superconductors with nodes in the gap dispersion. Second, optimally doped cuprates in their normal state are strange metals whose behaviour is governed by strong interactions⁶⁸. In previous models, the role of these properties has not been addressed. We also note that our work points out that it is the local uniformity of the device, rather than the absolute gap, that matters. After all, in all SNSPDs, the gap is suppressed by using a bias current. As long as the device is highly uniform, this suppression can, in principle, be near perfect, permitting even a high-gap device to exhibit a single-photon response.

Conclusions

In this work, we demonstrated single-photon detection in high- T_c cuprate SNWs at temperatures up to 25 K. Our results refute the

long-standing opinion that large-gap superconductors have lower sensitivity to low-energy photons. Additionally, it is surprising that these materials, which are very different from past examples, also exhibit single-photon detection, suggesting that the detection mechanism may need to be reconsidered. Finally, our work opens prospects of further developments in the high- T_c quantum sensors and their integration into on-chip photonic quantum information circuits.

Online content

Any methods, additional references, Nature Portfolio reporting summaries, source data, extended data, supplementary information, acknowledgements, peer review information; details of author contributions and competing interests; and statements of data and code availability are available at https://doi.org/10.1038/s41565-023-01325-2.

References

- Knill, E., Laflamme, R. & Milburn, G. J. A scheme for efficient quantum computation with linear optics. *Nature* 409, 46–52 (2001).
- Varnava, M., Browne, D. E. & Rudolph, T. How good must single photon sources and detectors be for efficient linear optical quantum computation? *Phys. Rev. Lett.* 100, 060502 (2008).
- 3. Spring, J. B. et al. Boson sampling on a photonic chip. Science **339**, 798–801 (2013).
- 4. Tillmann, M. et al. Experimental boson sampling. *Nat. Photonics* **7**, 540–544 (2013).
- Carolan, J. et al. Universal linear optics. Science 349, 711–716 (2015).
- 6. Wang, H. et al. High-efficiency multiphoton boson sampling. *Nat. Photonics* **11**, 361–365 (2017).
- Paterova, A. V., Yang, H., An, C., Kalashnikov, D. A. & Krivitsky, L. A. Tunable optical coherence tomography in the infrared range using visible photons. Quantum Sci. Technol. 3, 025008 (2018).
- Bhargav, A. M., Rakshit, R. K., Das, S. & Singh, M. Metrology perspective of single-photon detectors: review on global calibration methods. Adv. Quantum Technol. 4, 2100008 (2021).
- Giovannetti, V., Lloyd, S. & Maccone, L. Advances in quantum metrology. Nat. Photonics 5, 222–229 (2011).
- Hadfield, R. H. Single-photon detectors for optical quantum information applications. Nat. Photonics 3, 696–705 (2009).
- 11. Valivarthi, R. et al. Quantum teleportation across a metropolitan fibre network. *Nat. Photonics* **10**, 676–680 (2016).
- Liao, S.-K. et al. Satellite-relayed intercontinental quantum network. *Phys. Rev. Lett.* **120**, 030501 (2018).
- 13. Gisin, N. & Thew, R. Quantum communication. *Nat. Photonics* **1**, 165–171 (2007).
- Zhao, Q.-Y. et al. Single-photon imager based on a superconducting nanowire delay line. *Nat. Photonics* 11, 247–251 (2017).
- Xia, F. et al. Short-wave infrared confocal fluorescence imaging of deep mouse brain with a superconducting nanowire single-photon detector. ACS Photonics 8, 2800–2810 (2021).
- Ozana, N. et al. Superconducting nanowire single-photon sensing of cerebral blood flow. *Neurophotonics* 8, 035006 (2021).
- Li, L. & Davis, L. M. Single photon avalanche diode for single molecule detection. Rev. Sci. Instrum. 64, 1524–1529 (1993).
- Bao, Z. et al. Laser ranging at few-photon level by photon-number-resolving detection. *Appl. Opt.* 53, 3908–3912 (2014).
- Zhu, J. et al. Demonstration of measuring sea fog with an SNSPD-based lidar system. Sci. Rep. 7, 1–7 (2017).
- Carp, S. A. et al. Diffuse correlation spectroscopy measurements of blood flow using 1064nm light. *J. Biomed. Opt.* 25, 097003 (2020).

- Poon, C.-S. et al. First-in-clinical application of a time-gated diffuse correlation spectroscopy system at 1064 nm using superconducting nanowire single photon detectors in a neuro intensive care unit. *Biomed. Opt. Express* 13, 1344–1356 (2022).
- 22. Ota, R. Photon counting detectors and their applications ranging from particle physics experiments to environmental radiation monitoring and medical imaging. *Radiol. Phys. Technol.* **14**, 134–148 (2021).
- Ceccarelli, F. et al. Recent advances and future perspectives of single-photon avalanche diodes for quantum photonics applications. Adv. Quantum Technol. 4, 2000102 (2021).
- Kim, J., Takeuchi, S., Yamamoto, Y. & Hogue, H. H. Multiphoton detection using visible light photon counter. *Appl. Phys. Lett.* 74, 902–904 (1999).
- 25. Berggren, K. & Nam, S.-W. in Single-Photon Generation and Detection Vol. 45 (eds Migdall, A. et al.) Ch. 6 (Elsevier, 2013).
- Wolff, M. A. et al. Broadband waveguide-integrated superconducting single-photon detectors with high system detection efficiency. Appl. Phys. Lett. 118, 154004 (2021).
- Reddy, D. V., Nerem, R. R., Nam, S. W., Mirin, R. P. & Verma, V. B. Superconducting nanowire single-photon detectors with 98% system detection efficiency at 1550 nm. *Optica* 7, 1649–1653 (2020).
- Hu, P. et al. Detecting single infrared photons toward optimal system detection efficiency. Opt. Express 28, 36884–36891 (2020).
- Chang, J. et al. Detecting telecom single photons with 99.5% system detection efficiency and high time resolution. APL Photonics 6, 036114 (2021).
- 30. Hochberg, Y. et al. Detecting sub-GeV dark matter with superconducting nanowires. *Phys. Rev. Lett.* **123**, 151802 (2019).
- Korzh, B. et al. Demonstration of sub-3 ps temporal resolution with a superconducting nanowire single-photon detector. *Nat. Photonics* 14, 250–255 (2020).
- Cherednichenko, S., Acharya, N., Novoselov, E. & Drakinskiy, V. Low kinetic inductance superconducting MgB₂ nanowires with a 130 ps relaxation time for single-photon detection applications. Supercond. Sci. Technol. 34, 044001 (2021).
- Engel, A., Renema, J. J., Il'in, K. & Semenov, A. Detection mechanism of superconducting nanowire single-photon detectors. Supercond. Sci. Technol. 28, 114003 (2015).
- Natarajan, C. M., Tanner, M. G. & Hadfield, R. H. Superconducting nanowire single-photon detectors: physics and applications. Supercond. Sci. Technol. 25, 063001 (2012).
- 35. Sherman, N. Superconducting nuclear particle detector. *Phys. Rev. Lett.* **8**, 438 (1962).
- Johnson, M., Herr, A. & Kadin, A. Bolometric and nonbolometric infrared photoresponses in ultrathin superconducting nbn films. J. Appl. Phys. 79, 7069–7074 (1996).
- Semenov, A. D., Gol'tsman, G. N. & Korneev, A. A. Quantum detection by current carrying superconducting film. *Phys. C Supercond.* 351, 349–356 (2001).
- Gol'Tsman, G. et al. Picosecond superconducting single-photon optical detector. Appl. Phys. Lett. 79, 705–707 (2001).
- 39. Shibata, H. Review of superconducting nanostrip photon detectors using various superconductors. *IEICE Trans. Electron.* **104**, 429–434 (2021).
- Velasco, A. E. et al. High-operating-temperature superconducting nanowire single photon detectors. In Conference on Lasers and Electro-optics QELS_Fundamental Science, FW4C-5 (Optical Society of America, 2016).
- Andersson, E., Arpaia, R., Trabaldo, E., Bauch, T. & Lombardi, F. Fabrication and electrical transport characterization of high quality underdoped YBa₂Cu₃O_{7-δ} nanowires. Supercond. Sci. Technol. 33, 064002 (2020).

- Ejrnaes, M. et al. Observation of dark pulses in 10 nm thick YBCO nanostrips presenting hysteretic current voltage characteristics. Supercond. Sci. Technol. 30, 12LTO2 (2017).
- 43. Lyatti, M. et al. Energy-level quantization and single-photon control of phase slips in YBa₂Cu₃O_{7-x} nanowires. *Nat. Commun.* **11**, 763 (2020).
- 44. Frenkel, A. et al. Optical response of nongranular high T_c $Y_1Ba_2Cu_3O_{7-x}$ superconducting thin films. *J. Appl. Phys.* **67**, 3054–3068 (1990).
- Amari, P. et al. High-temperature superconducting nanomeanders made by ion irradiation. Supercond. Sci. Technol. 31, 015019 (2018).
- Couëdo, F. et al. Dynamic properties of high-T₀ superconducting nano-junctions made with a focused helium ion beam. Sci. Rep. 10, 1–9 (2020).
- Sterpetti, E., Biscaras, J., Erb, A. & Shukla, A. Comprehensive phase diagram of two-dimensional space charge doped Bi₂Sr₂CaCu₂O_{8+x}. Nat. Commun. 8, 1–8 (2017).
- Wang, F., Biscaras, J., Erb, A. & Shukla, A. Superconductor-insulator transition in space charge doped one unit cell Bi₂₁Sr₁₉CaCu₂O_{8+x}. Nat. Commun. 12, 1–6 (2021).
- Sandilands, L. J. et al. Origin of the insulating state in exfoliated high-T_c two-dimensional atomic crystals. *Phys. Rev. B* 90, 081402 (2014).
- Vasquez, R. Intrinsic photoemission signals, surface preparation, and surface stability of high temperature superconductors.
 J. Electron Spectrosc. Relat. Phenom. 66, 209–222 (1994).
- 51. Poccia, N. et al. Evolution and control of oxygen order in a cuprate superconductor. *Nat. Mater.* **10**, 733–736 (2011).
- 52. Zhao, S. Y. F. et al. Sign-reversing Hall effect in atomically thin high-temperature $Bi_{21}Sr_{19}CaCu_{2.0}O_{8+\delta}$ superconductors. *Phys. Rev. Lett.* **122**, 247001 (2019).
- 53. Yu, Y. et al. High-temperature superconductivity in monolayer $Bi_2Sr_2CaCu_2O_{8+5}$. Nature **575**, 156–163 (2019).
- 54. Cybart, S. A. et al. Nano Josephson superconducting tunnel junctions in $YBa_2Cu_3O_{7-\delta}$ directly patterned with a focused helium ion beam. *Nat. Nanotechnol.* **10**, 598–602 (2015).
- Martinez, G. D., Buckley, D., Charaev, I., Dow, D. E. & Berggren, K. K. Superconducting nanowire fabrication using dislocation engineering. In 2019 IEEE MIT Conference (URTC) 1–4 (IEEE, 2019).
- Gozar, A., Litombe, N. E., Hoffman, J. E. & Božović, I. Optical nanoscopy of high T_c cuprate nanoconstriction devices patterned by helium ion beams. *Nano Lett.* 17, 1582–1586 (2017).
- Seifert, P. et al. A high-T_c Van der Waals superconductor based photodetector with ultra-high responsivity and nanosecond relaxation time. 2D Mater. 8, 035053 (2021).
- Gozar, A. et al. High-temperature interface superconductivity between metallic and insulating copper oxides. *Nature* 455, 782–785 (2008).
- Logvenov, G., Gozar, A. & Bozovic, I. High-temperature superconductivity in a single copper–oxygen plane. Science 326, 699–702 (2009).
- Skocpol, W., Beasley, M. & Tinkham, M. Self-heating hotspots in superconducting thin-film microbridges. J. Appl. Phys. 45, 4054–4066 (1974).
- 61. Chiles, J. et al. Superconducting microwire detectors based on WSi with single-photon sensitivity in the near-infrared. *Appl. Phys. Lett.* **116**, 242602 (2020).
- 62. Caloz, M. et al. Intrinsically-limited timing jitter in molybdenum silicide superconducting nanowire single-photon detectors. *J. Appl. Phys.* **126**, 164501 (2019).
- 63. Cheng, R. et al. A 100-pixel photon-number-resolving detector unveiling photon statistics. *Nat. Photonics* **17**, 112–119 (2023).

- Kerman, A. J., Yang, J. K., Molnar, R. J., Dauler, E. A. & Berggren, K. K. Electrothermal feedback in superconducting nanowire single-photon detectors. *Phys. Rev. B* 79, 100509 (2009).
- 65. Marsili, F. et al. Detecting single infrared photons with 93% system efficiency. *Nat. Photonics* **7**, 210–214 (2013).
- 66. Semenov, A. D. Superconducting nanostrip single-photon detectors some fundamental aspects in detection mechanism, technology and performance. *Supercond. Sci. Technol.* **34**, 054002 (2021).
- Keimer, B., Kivelson, S. A., Norman, M. R., Uchida, S. & Zaanen, J. From quantum matter to high-temperature superconductivity in copper oxides. *Nature* 518, 179–186 (2015).
- Varma, C. M. Colloquium: linear in temperature resistivity and associated mysteries including high temperature superconductivity. Rev. Mod. Phys. 92, 031001 (2020).

69. Zhou, X. et al. High-temperature superconductivity. *Nat. Rev. Phys.* **3**, 462–465 (2021).

Publisher's note Springer Nature remains neutral with regard to jurisdictional claims in published maps and institutional affiliations.

Springer Nature or its licensor (e.g. a society or other partner) holds exclusive rights to this article under a publishing agreement with the author(s) or other rightsholder(s); author self-archiving of the accepted manuscript version of this article is solely governed by the terms of such publishing agreement and applicable law.

@ The Author(s), under exclusive licence to Springer Nature Limited 2023

Methods

Fabrication of BSCCO photodetectors

To fabricate SNWs out of BSCCO we mechanically exfoliated bulk crystals and deposited cleaved flakes onto polydimethylsiloxane (PDMS) polymer stamps attached to the glass slide. To avoid the degradation of the flakes, the exfoliation was done in the inert atmosphere of the argon-filled glovebox. The flakes were then transferred onto prepatterned Si/SiO₂ substrates with ultra-flat titanium/gold contacts and covered by relatively thick (-50 nm) slabs of hBN.

The fabrication of ultra-flat contacts comprised several steps and relied on a lift-off-free procedure. First, thin layers of titanium (3 nm) and gold (25 nm) were evaporated onto the $\mathrm{Si/SiO_2}$ wafer. Next, negative e-beam lithography was used to define a mask for selective removal of the metal outside the designated contact areas. This removal was done by a combination of argon and oxygen etching. Resist residues were further removed by immersing the substrates into N-methyl-pyrrolidone (NMP) solution and subsequent aggressive stripping using extensive oxygen plasma cleaning. We intentionally increased the typical dwell time of the plasma cleaning to reduce the thickness of the gold layer to 20 nm.

To define superconducting SNWs out of prepared partially encapsulated BSCCO devices by He⁺ ion beam, we first ran the simulation of the ion collision damage using SRIM software (Supplementary Information, section 1). This allowed us to estimate the characteristic doses needed to introduce a significant number of defects into the BSCCO crystal lattice and suppress superconductivity. Next, starting from the obtained values, we performed dose tests using a Zeiss Orion microscope with a Raith pattern generator and determined the optimum parameters needed to define the desired SNWs.

Fabrication of LSCO-LCO photodetectors

To fabricate SNWs out of LSCO–LCO bilayer we started from thin bilayer films grown by the atomic-layer-by-layer molecular beam epitaxy (ALL-MBE) technique (Supplementary Information, section 1). Titanium/gold contact pads were fabricated using standard e-beam lithography followed by metal deposition. To produce the SNWs out of LSCO–LCO bilayer films, another round of e-beam lithography was made, using high-resolution positive e-beam resist (ZEP520A). The patterns were then transferred onto the LSCO–LCO film by Ar⁺ milling at a beam voltage of 300 V and an argon flow of 9 sccm for 10 min. The residual resist was removed by immersing the substrate in the warm NMP solution.

After fabrication, we irradiated our SNWs with He $^+$ using a Zeiss Orion microscope equipped with a Raith pattern generator. The irradiation was realized through sweeping of the beam across the SNW area. The exposed area is a rectangle with approximate dimensions of $5 \times 5 \, \mu m^2$ (to cover the whole meander area). The beam spot is $-2 \, nm$. The dose varied in the range from 10^{15} to 10^{20} ions per cm 2 (Supplementary Information, section 3). The samples were then characterized using transport measurements to identify those with pronounced hysteresis in the I-V curves. For the photoresponse measurements, we chose the sample which featured the strongest hysteresis with the minimal suppression of I_c .

Data availability

The data reported in Figs. 2–4 can be found on Zenodo (https://doi. org/10.5281/zenodo.7501827). The other data that support the findings

of this study are available from the corresponding authors upon reasonable request.

Acknowledgements

Work in the P.J.H. group was partly supported through AFOSR grant FA9550-21-1-0319, through the NSF QII-TAQS programme (grant 1936263), and the Gordon and Betty Moore Foundation EPiQS Initiative through grant GBMF9463 to P.J.H. I.Y.P acknowledges support from the MIT undergraduate research opportunities programme and the Johnson & Johnson research scholars programme. K.K.B. and group members acknowledge support from Brookhaven Science Associates, LLC award number 030814-00001. K.W. and T.T. acknowledge support from JSPS KAKENHI (grant numbers 19H05790, 20H00354 and 21H05233). Thin-film synthesis and characterization at Brookhaven National Laboratory was supported by the US Department of Energy, Basic Energy Sciences, Materials Sciences and Engineering Division. H.X. was supported by the Gordon and Betty Moore Foundation's EPiQS Initiative through grant GBMF9074. O. Medeiros acknowledges funding from the NDSEG Fellowship Program. We acknowledge valuable discussions with S. Rescia (BNL) and G. Carini (BNL) and their significant help during the planning and development of this research work. The authors thank J. Daley and M. Mondol of the MIT Nanostructures laboratory for the technical support related to electron-beam fabrication and helium ion microscopy. We also thank F. Zhao (Harvard), Prof. Schilling (UZH) and M. Karmantsov (MMDES) for helpful discussions.

Author contributions

D.A.B. and I.C. conceived and designed the project. I.C. and D.A.B. performed transport measurements. I.C. performed the photoresponse measurements. D.A.B., I.C. and I.Y.P. fabricated the devices. B.A.B., M.C. and I.C. designed the readout circuit. O.M. simulated the readout circuit. I.C. and D.A.B. analysed the experimental data with help from I.B., P.J.-H. and K.K.B. I.D. provided BSCCO crystals. X.H., A.T.B. and I.B. synthesized and characterized the LSCO–LCO bilayer films. T.T. and K.W. provided high-quality hBN crystals. I.C. and D.A.B. wrote the manuscript with input from all coauthors. P.J.-H., I.B. and K.K.B. supervised the project. All authors contributed to discussions.

Competing interests

The authors declare no competing interests.

Additional information

Supplementary information The online version contains supplementary material available at https://doi.org/10.1038/s41565-023-01325-2.

Correspondence and requests for materials should be addressed to I. Charaev, D. A. Bandurin or K. K. Berggren.

Peer review information *Nature Nanotechnology* thanks Cheryl Feuillet-Palma and the other, anonymous, reviewer(s) for their contribution to the peer review of this work.

Reprints and permissions information is available at www.nature.com/reprints.